Photothermal Measurements of Internal Quantum and Energy Efficiencies of Semiconductor Photoelectrodes A Review

Andreas MANDELIS

Photoacoustic and Photothermal Sciences Laboratory, Department of Mechanical Engineering and Ontario Laser and Lightwave Research Center, University of Toronto, Toronto, Ontario, Canada M5S 1A4

Photothermal and photoacoustic detection of semiconductor photoelectrochemical interfaces can be utilized to yield information about the internal quantum and energy efficiencies of the photoelectrode electrochemical process. The theoretical foundations and progress in the experimental state-of-the-art in this field are reviewed. The importance of measurements in the characterization and/or optimization of energy conversion efficiencies of photoelectrochemical cells, as well as their contribution to our understanding of energy transfer physics at the illuminated interface, will be discussed further.

Keywords Internal quantum efficiency, internal energy efficiency, photoacoustic spectroscopy, photothermal thermistor spectroscopy, photothermal deflection spectroscopy, photoelectrochemistry, semiconductors, energy-transfer physics, interface, electrolyte, Peltier heat

1 Introduction

In recent years the popular analytical tools of photoacoustic (PA) and photothermal (PT) spectroscopies[1,2] have been increasingly applied to specific diagnostic tasks as non-intrusive probes. One of the most promising areas is that of the photoelectrochemical (PEC) semiconductor photoelectrode-electrolyte interface. A comprehensive review of other electrochemical investigations by the use of photothermal probes has recently appeared elsewhere.[3] The specific area of PA and PT studies of semiconducting photoelectrodes has been particularly rewarding, not only for the practical importance of such investigations in the optimization of PEC energy conversion devices, but also for their ability to open up new theoretical vistas toward the understanding of the PEC interface energy transfer physics. This task has been greatly facilitated by the advanced state of our understanding of the electrochemical behavior of many semiconductors[4] in relation to their energy band structures[5] and their optical properties.[6]

It is precisely our degree of understanding of the PEC response of semiconductors which has led to the impressive progress in our assessment of the value PAS and PTS as diagnostic tools yielding interfacial energetics information unobtainable by other techniques. Although more investigations are clearly needed to exploit the full power of these non-intrusive analytical methods, it appears at this time that unequivocal statements can be made concerning their ability to monitor and measure internal quantum and energy efficiencies. Valuable information about other dynamic processes at the semiconductor-electrolyte interface may also be obtained by combining photothermal techniques with other optical, electronic and/or electrochemical probes, such as measurement of the electrochemical heat of reaction (Peltier heat).

In this review, important progress to-date in the field of PA and PT applications to semiconductor-electrolyte photointerfaces is described. The theoretical founda-

tions of the energy-transfer physics is presented in Section 2, followed by phenomenological signal theory for the three major photothermal techniques; photothermal thermistor spectroscopy (PTS); photoacoustic spectroscopy (PAS); and photothermal deflection (or mirage-effect) spectroscopy (PDS). Experimental results highlighting progress in the measurements of the internal quantum and energy efficiencies of various semiconductor PEC cells are discussed in Section 3. The measurements of other interfacial parameters as a result of combination experiments are also presented in that Section. This involves progress in the by-product measurement of the electrochemical Peltier heat (EPH). Finally Section 4 is a summary of the state-of-the-art and a brief discussion of the main relative advantages of the major photothermal investigation techniques with regard to the semiconductor PEC interface characterization.

2 Energy-Transfer Physics at Semiconductor-Electrolyte Interfaces

2·1 Measurement of internal quantum efficiency

Photothermal probes at the semiconductor-electrolyte interface are sensitive to heat released in the surface or bulk or electrolytic vicinity of the photoelectrode following optical excitation of the semiconductor. The significant thermal generation processes at the working electrode (WE)-electrolyte interface can be described[7,8] with the aid of Fig. 1. In making quantitative predictions about the contribution of each thermal generation mechanism to the photothermal signal, the important distinction of the WE being under bias or under load must be made.[9]

The heat generation sources are follows:

i) Following optical absorption, a nonradiative intraband deexcitation of hot electrons from excited states in the conduction band (CB) to states near the bandedge yields a photothermal signal component,
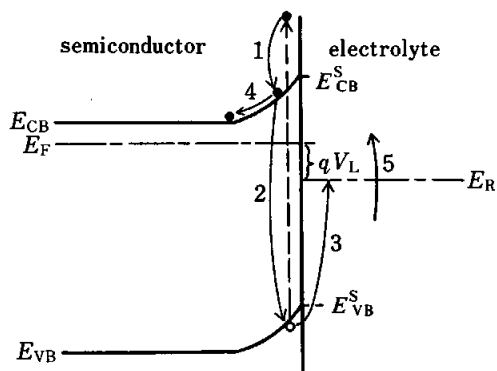

Fig. 1   Heat-generating mechanisms contributing to the photothermal signal at the working semiconductor photoelectrode-electrolyte interface.[9] See text for an explanation of the five heat sources (S_j; $j=1-5$).

$$S_1 = KN(h\nu - E_g), \qquad (1)$$

where E_g is the optical bandgap of the semiconductor WE, and K is a proportionality constant dependent on the particular PEC cell geometry and photothermal technique used. N is the peak photon absorption rate (photons/s). All optically generated CB electrons are assumed to undergo the fast ($\sim$ps) transitions described by Eq. (1).

ii) Nonradiative interband deexcitation between the CB and the valence band (VB) in the form of electron-hole recombination contributes a signal component, under bias, of magnitude

$$S_2^{(B)} = KN(1 - \eta_{Qi}^{(B)})E_g, \qquad (2)$$

where $\eta_{Qi}^{(B)}$ is the internal quantum efficiency of the photoelectrode reaction under bias, defined by

$$\eta_{Qi}^{(B)} = \frac{I_B}{N}. \qquad (3)$$

In Eq. (3), I_B is the peak cell photocurrent, the unit for which has been chosen to be electrons/s, unless otherwise noted. It should be noticed that a photothermal probe is only sensitive to the internal quantum efficiency, η_{Qi}, and *not* to the more common external quantum efficiency, η_{Qe}, which is measurable by nonthermal (usually optical) techniques.[10] The former quantity involves the number N of absorbed photons by the photoelectrode, rather than that incident on the electrode. Therefore a feature common to all photothermal quantum efficiency determination schemes is that they do not require knowledge of the incident light intensity (*i.e.* calibration taking account of the surface reflectivity). Under external load conditions, Eq. (2) must be replaced by

$$S_2^{(L)} = KN(1 - \eta_{Qi;ac}^{(L)} - \eta_{Qi;dc}^{(L)})E_g, \qquad (4)$$

where $\eta_{Qi;ac}^{(L)} \equiv I_L^{ac}/N$ is the ac component of the cell internal quantum efficiency, and I_L^{ac} is the ac component of the cell photocurrent. Similarly, $\eta_{Qi;dc}^{(L)} \equiv I_L^{dc}/N$ is the dc component of the cell internal quantum efficiency, and I_L^{dc} is the dc component of the cell photocurrent.

iii) Electron injection from the electrolyte into the VB (for n-type photoelectrodes) gives, under bias,

$$S_3^{(B)} = KN\eta_{Qi}^{(B)}(E_R - E_{VB}^S), \qquad (5)$$

where E_R is the redox level of the electrolyte (*vs.* reference) and E_{VB}^S is the valence-band energy level at the surface (*vs.* reference). Under load conditions, the following expression must replace Eq. (5):

$$S_3^{(L)} = 2KN\eta_{Qi;ac}^{(L)}(E_R - E_{VB}^S). \qquad (6)$$

The factor of 2 in Eq. (6) is due to the ac nature of $\eta_{Qi;ac}^{(L)}$ calculated from photothermal signals integrated

over one modulation cycle (period).

(iv) The carrier separation in the depletion layer, where carriers are transported from the surface to the semiconductor bulk, while losing energy under the influence of the built-in electric field, yields for the biased electrode

$$S_4^{(B)} = KN\eta_{Qi}^{(B)}|e|(V-V_{FB}),\qquad(7)$$

where $|e|$ is the absolute value of the electronic charge, V the applied bias (vs. reference), and V_{FB} the flatband potential (vs. reference). Equation (7) does not include the heat balance at the back ohmic contact (Peltier heat), and is generally valid only for low-resistivity electrodes, where the semiconductor Fermi level is close to the conduction bandedge (a good approximation for n-type materials). Under load conditions the situation is more complex,

$$S_4^{(L)} = KN\,[2\eta_{Qi;ac}^{(L)}(E_{CB}^S-E_R-E_L^{dc})-2\eta_{Qi;dc}^{(L)}\,E_L^{dc}],\qquad(8)$$

where E_{CB}^S is the CB energy level at the photoelectrode surface (vs. reference); $E_L^{dc}\equiv|e|V_L^{dc}$, where V_L^{dc} is the dc potential drop across the external load attached to the cell; $E_L^{ac}\equiv|e|V_L^{ac}$, where V_L^{ac} is the ac component of the external potential load drop. The origin of the factors of 2 is similar to that discussed under source (iii) above.

v) The free-energy change of the redox reaction, a significant component of the electrochemical Peltier heat (EPH)[11], gives for the biased cell

$$S_5^{(B)} = KN\eta_{Qi}^{(B)}\Delta G,\qquad(9)$$

where ΔG is the free-energy change of the WE redox reaction. Under load conditions Eq. (9) is replaced by

$$S_5^{(L)} = 2KN\eta_{Qi;ac}^{(L)}\Delta G.\qquad(10)$$

The resistive heating of the photoelectrode and electrolyte can be ignored for a low-resistivity semiconductor and a non-dilute electrolyte. Summing up, the five partial photothermal signals for a cell under bias, Eqs. (1), (2), (5), (7) and (9) give the total signal under bias V,

$$S^{(B)}(V)=KN[(h\nu-E_g)+(1-\eta_{Qi}^{(B)})E_g+\eta_{Qi}^{(B)}(E_R-E_{VB}^S)$$
$$+\eta_{Qi}^{(B)}|e|(V-V_{FB})+\eta_{Qi}^{(B)}\Delta G].\qquad(11)$$

If the cell is at open circuit (OC), $I_B=0$ in Eq. (3), so that $\eta_{Qi}^{(B)}=0$. In that limit, the total photothermal signal $S_{OC}^{(B)}$ is

$$S_{OC}^{(B)} = KNh\nu.\qquad(12)$$

The open-circuit photothermal signal provides a convenient normalization means under bias, since under OC conditions all of the absorbed optical energy is converted to heat at the photoelectrode-electrolyte

interface (this assumes negligible semiconductor luminescence). The fact that neither $S^{(B)}(V)$, Eq. (11), nor $S_{OC}^{(B)}$, Eq. (12), is sensitive to the absolute number of photons incident upon the WE, but only to the absorbed fraction N, causes the photothermal signal to depend on the internal quantum efficiency of the photoelectrode reaction. Taking into account that K and N do not depend upon whether the system is at OC or under bias, Eqs. (11) and (12) yield an expression for the normalized photothermal signal under bias,

$$S_n^{(B)}(V)\equiv\frac{S^{(B)}(V)}{S_{OC}^{(B)}}=[(h\nu-E_g)+(1-\eta_{Qi}^{(B)})E_g$$
$$+\eta_{Qi}^{(B)}(E_R-E_{VB}^S)+\eta_{Qi}^{(B)}|e|(V-V_{FB})+\eta_{Qi}^{(B)}\Delta G]/h\nu.\qquad(13)$$

Considering that the cell photocurrent and, hence, quantum efficiency are independent of the voltage at a large reverse bias, a variation of V within this region yields a local slope of Eq. (13),

$$\frac{\partial S_n^{(B)}(V)}{\partial(V-V_{FB})}=\frac{|e|\eta_{max}^{(B)}}{h\nu},\qquad(14)$$

where $\eta_{max}^{(B)}$ is defined as the maximum internal quantum efficiency of the PEC cell under a given set of experimental bias conditions. If the unit of $h\nu$ is chosen to be eV, $|e|$ may be set equal to one in Eq. (14). This suggests a method for measuring the internal quantum efficiency of the PEC cell under monochromatic excitation from the slope of the normalized photothermal signal vs. the applied bias.

Once $\eta_{max}^{(B)}$ has been found, it is possible to obtain an approximate value for the energy change in the system due to the redox reaction, namely, an estimate for $(E_R-E_{VB}^S)+\Delta G$, where $(E_R-E_{VB}^S)$ is the change in energy of an electron moving from the redox level to the VB, and ΔG is the free-energy change of the WE reaction. The quantity $(E_R-E_{VB}^S)+\Delta G$ is experimentally determined from the ordinate intercept of the $S_n^{(B)}(V)$ vs. $(V-V_{FB})$ curve, which is given by

$$S_{intercept}^{(B)}=[h\nu-\eta_{max}^{(B)}E_g+\eta_{max}^{(B)}(E_R-E_{VB}^S)+\eta_{max}^{(B)}\Delta G]/h\nu.\qquad(15)$$

Since the values of $h\nu$, E_g and $\eta_{max}^{(B)}$ are nominally known, the value of $(E_R-E_{VB}^S)+\Delta G$ can be derived.

In order to find the non-maximum internal quantum efficiency $\eta_{Qi}^{(B)}$ as a function of applied bias, a general expression for $\eta_{Qi}^{(B)}$ may be written[8] in terms of $\eta_{max}^{(B)}$,

$$\frac{\eta_{Qi}^{(B)}(V)}{i_B(V)}=\frac{1}{N}\left(\frac{N_A}{F}\right)=\frac{\eta_{max}^{(B)}}{i_{max}}$$

or

$$\eta_{Qi}^{(B)}(V)=\left[\frac{i_B(V)}{i_{max}}\right]\eta_{max}^{(B)},\qquad(16)$$

where N_A is Avogadro's number, F is one faraday ($=10^4$ C/mol), $i_B(V)$ is the cell photocurrent (A) at bias V and i_{max} is the maximum photocurrent corresponding to $\eta_{max}^{(B)}$.

2·2 Measurement of internal energy efficiency

In addition to providing a measurement method for the internal quantum efficiency of the photoelectrode reaction of a PEC cell, photothermal measurements further allow the determination of the internal energy conversion efficiency, defined as

$$\eta_{Ei}^{(j)} \equiv \frac{W_{out}^{(j)}}{W_{in}}, \tag{17}$$

where W_{out} and W_{in} are the photoelectrode chemical or the electrical power output and the optical power input, respectively, and superscript (j) denotes the bias (B) or load (L) conditions. The conventional method of finding the *external* energy efficiency involves measuring the electrical output power to the cell load and dividing this by the optical power incident on the photoelectrode. The energy efficiency, thus measured, depends on the value of the load; there will be some optimum load which results in a maximum energy efficiency.[12] When use is made of photothermal data obtained by changing the PEC cell bias, the single electrode, monochromatic internal energy (conversion) efficiency may be defined as

$$\eta_{Ei}^{(B)} = \eta_{Qi}^{(B)}\left[\frac{E_g-(E_R+E_{VB}^S)}{h\nu}\right]. \tag{18}$$

Equation (18) can assume a simpler form,

$$\eta_{Ei}^{(B)} \approx \eta_{Qi}^{(B)}\left(\frac{E_{FB}-E_R}{h\nu}\right), \tag{19}$$

in cases where $E_g-E_{VB}^S \approx E_{FB}$ in Fig. 1. Equation (19) with $\eta_{Qi}^{(B)}=1.0$ represents the ideal energy efficiency[7] and ($E_{FB}-E_R$) corresponds to the maximum photo-voltage in the PEC cell. Formally, Eq. (18) may be derived from Eqs. (13) and (15), upon substituting,

$$\eta_{Ei}^{(B)} = 1-S_n^{(B)}(V_{FB})-\eta_{Qi}^{(B)}\left(\frac{\Delta G}{h\nu}\right), \tag{20}$$

where $S_n^{(B)}(V)|_{V=V_{FB}}=S_{intercept}^{(B)}$ from Eq. (15). Definition (18) is, thus, consistent with that given by Fujishima *et al.*[11] For a general photothermal measurement at the semiconductor-electrolyte interface, the heat generation model for a PEC cell connected to an external load resistor (Section 2·1) applies and yields

$$S_n^{(L)}(V) \equiv \frac{S^{(L)}(V)}{S_{OC}^{(L)}} = [h\nu+(\eta_{Qi;ac}^{(L)}-\eta_{Qi;dc}^{(L)})E_g$$

$$-2(\eta_{Qi;ac}^{(L)}E_L^{dc}+\eta_{Qi;dc}^{(L)}E_L^{ac})+2\eta_{Qi;ac}^{(L)}\Delta G]/h\nu, \tag{21}$$

where all of the quantities were defined previously. The basic relation used to obtain the internal energy efficiency under load, Eq. (17), may be written as[8]

$$\eta_{Ei}^{(L)} = 1-S_n^{(L)}(V)=[2(\eta_{Qi;ac}^{(L)}E_L^{dc}+\eta_{Qi;dc}^{(L)}E_L^{ac})$$

$$-(\eta_{Qi;ac}^{(L)}-\eta_{Qi;dc}^{(L)})E_g-2\eta_{Qi;ac}^{(L)}\Delta G]/h\nu. \tag{22}$$

It should be noticed that the photothermal determination of $\eta_{Ei}^{(L)}$, in its most general form, requires knowledge of both the dc and ac quantum efficiencies under load, $\eta_{Qi;dc}^{(L)}$ and $\eta_{Qi;ac}^{(L)}$, as well as the free-energy change of the WE redox reaction, ΔG. In what follows we review and examine how the general energy-transfer formulations presented above have been, and can be, used with particular photothermal detection schemes and with specific semiconductor photoelectrodes.

3 Photothermal Investigations of Internal Quantum and/or Energy Efficiencies at Semiconductor-Electrolyte Interfaces

3·1 Photothermal thermistor spectroscopy (PTS)

Historically, the first quantitative photothermal investigations of semiconductor electrodes were performed using photothermal thermistor spectroscopy (PTS). Therefore, the salient features of this technique are examined first. Figure 2 shows a typical experimental set-up for this kind of detection. The method involves the recording of PT responses both under bias and under OC conditions. A thermistor measures the dc temperature change ΔT (with respect to the temperature ΔT_{ref} of a reference thermistor) in the vicinity of the WE due to a step-input optical excitation.[11] The thermistor signal at bias V is then normalized by the OC temperature, ΔT_{OC}. A calorimetric thermodynamic analysis of the temperature signal due to the enthalpy change during an electrochemical reaction[14] leads to a particular form of Eq. (13)[11],

$$E\left(\frac{\Delta T}{\Delta T_{OC}}\right)=\eta_{Qi}^{(B)}(V-V_{FB})+\frac{1}{N\tau}(Q_{SC}+T\Delta S), \tag{23}$$

where $E \equiv (h\nu/|e|)$ (eV) is a measure of the energy absorbed per incident photon in a semiconductor electrode capable of an average absorption rate N (photons/s), illuminated with a monochromatic optical pulse of energy $h\nu$ (J) and duration τ (s). In Eq. (23) the free-energy change of the WE redox reaction ΔG has been written in terms of the change in entropy ΔS of the reaction,

$$\Delta G=T\Delta S. \tag{24}$$

The lumped quantity, Q_{SC} (eV), corresponds to heat evolved in the semiconductor *via* recombination and nonradiative processes,
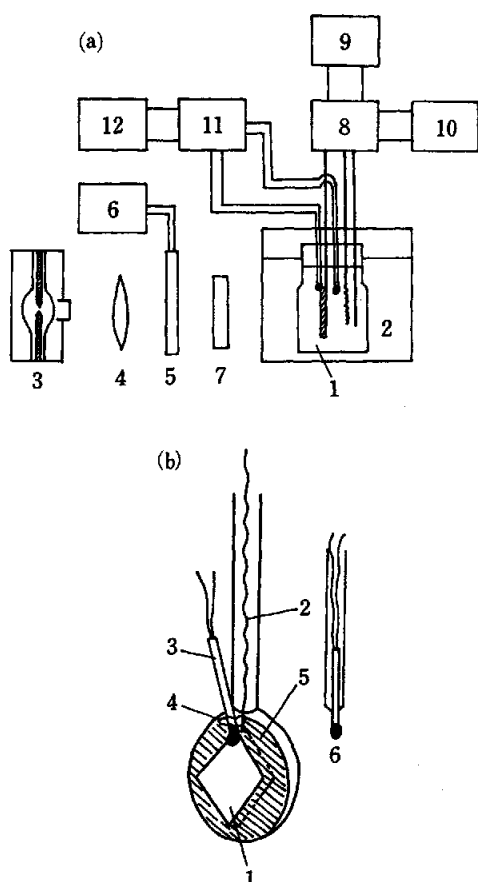
(a)

(b)

Fig. 2 (a) PTS measurement assembly.[13] 1, cell; 2, water bath; 3, 500 W Hg lamp; 4, lens; 5, shutter; 6, timer; 7, filter; 8, potentiostat; 9, potential sweeper; 10, X-Y recorder; 11, d.c. bridge; 12, polyrecorder (reprinted by permission of the Chemical Society of Japan). (b) Detector head details. 1, semiconductor crystal; 2, Cu lead wire; 3, thermistor; 4, silicone rubber; 5, epoxy resin; 6, reference thermistor. Light irradiates only the semiconductor surface and not the thermistors. The contact to the electrode and the thermistor is insulated from the solution by a thin layer of epoxy cement (reprinted by permission of the Electrochemical Society, Inc.).[11]

$$Q_{SC} \equiv \frac{N\tau}{|e|}\left\{h\nu - \eta_{Qi}^{(B)}\left[E_g - (E_R - E_{VB}^S)\right]\right\}. \qquad (25)$$

Equation (23) is obtained under the assumptions that the heat lost by conduction from the electrode and Joule heating of the electrolyte are negligible. These assumptions are valid for typical photothermal electrochemical processes (ΔT on the order of millidegrees and very low resistance of non-dilute electrolytes). Figure 3 shows a typical plot of data from a CdS single-crystal electrode illuminated in a sodium sulfite aqueous solution.[13] The anodic photocurrent curve shown exhibits saturation throughout the entire linear region of the PT signal, in agreement with the model leading to Eq. (14). Under large reverse bias conditions, the internal quantum efficiency is expected to be independent of the bias and to be maximum. The
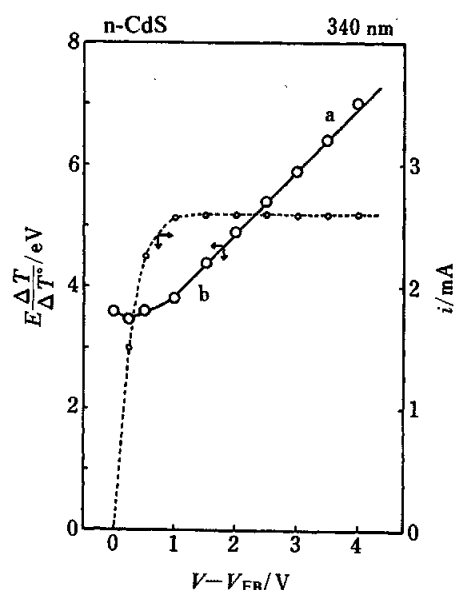

Fig. 3 (a) Normalized PTS signal vs. potential for a n-CdS single crystal electrode in 0.1 M Na_2SO_3 and 0.2 M Na_2SO_4. Irradiation conditions: λ=340 nm, E=3.6 eV, τ=20 s. (b) Photocurrent for the n-CdS PEC cell (reprinted by permission of the Chemical Society of Japan).[13]
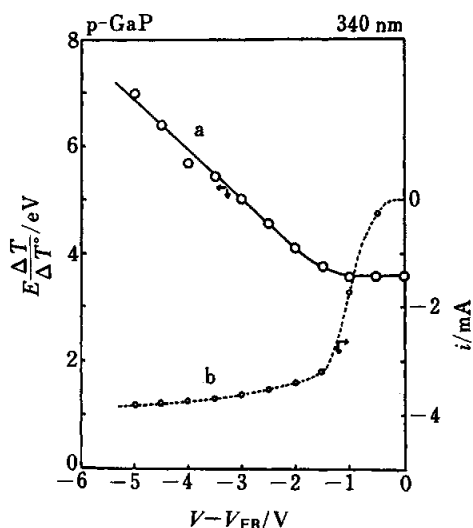

Fig. 4 (a) Normalized PTS signal vs. potential for a p-GaP single crystal electrode in 0.5 M H_2SO_4. Irradiation conditions: same as in Fig. 3. (b) Photocurrent for the p-GaP PEC cell (reprinted by permission of the Chemical Society of Japan).[13]

slope of the linear region of curve (a), Fig. 3, was found[13] to be 1.0, thus indicating that the quantum efficiency of the oxidation of sulfite ions on the illuminated n-CdS photoelectrode is unity. For a p-type semiconductor the photocurrent is mainly cathodic. Figure 4 shows plots equivalent to Fig. 3 pertaining to the application of the PTS technique to a p-GaP single crystal photoelectrode in a sulfuric acid electrolyte.[13] From the linear region of curve (a) it was

possible to obtain $\eta^{(B)}_{max}=0.80$ for the hydrogen evolution reaction. Fujishima et al.[13] measured the maximum internal quantum efficiencies of several photoelectrodes using PTS and compared their results with those obtained actinometrically. The comparison is shown in Table 1. It is interesting to note that the p-GaAs, 0.5 M H_2SO_4 system did not exhibit cathodic photocurrent saturation, nor a linear region in the $E(\Delta T/\Delta T_{OC})$ vs. $(V-V_{FB})$ plot. For this reason the possible range of $\eta^{(B)}_{max}$ was estimated to be between 0.80 and 1.00 in Table 1. With the aid of the model of Fig. 1, unity internal quantum efficiency indicates that all photoexcited electrons in the conduction band move

from the surface of the semiconductor into the bulk through the space charge layer giving rise to heat generation. A smaller value for $\eta^{(B)}_{Qi}$ indicates that an accordingly smaller fraction of the photoexcited electrons ultimately reaches the bulk, thus contributing to a smaller photocurrent. Therefore, it is expected that for simple redox systems the internal quantum efficiency maximum is unity. Maeda et al.[15] have shown, however, that $\eta^{(B)}_{Qi}>1$ is possible in cases involving current doubling reactions. In the energy diagram of Fig. 5 the situation is depicted for both n- and p-type photoelectrodes. For an n-type semiconductor, a current doubling reagent R is first reduced by a photogenerated hole in the valence band to $R^{\ddagger}$, which subsequently injects an electron into the conduction band, Fig. 5(a). For a p-type semiconductor, a current doubling reagent, X_2, is first reduced by a photogenerated electron in the conduction band, resulting in

Table 1 Comparison of quantum efficiencies at 340 nm[13]

Electrode	η_t	η_a	Electrolyte
n-CdS s	1.00	1.00	Na_2SO_3
n-CdS p	0.67	0.67-0.70	Na_2SO_3
n-CdSe s	0.42	0.40-0.42	Na_2S
n-GaP s	0.85	0.62	Na_2S
n-GaAs s	0.80	0.47-0.49	Na_2S
n-TiO$_2$ s	0.70	0.70	H_2SO_4
n-ZnO p	0.85	0.76-0.78	Na_2SO_4
n-MoS$_2$ s	1.00	0.54	Na_2SO_4
p-GaP s	0.80	0.60-0.66	H_2SO_4
p-GaAs s	0.80-1.00	0.56-0.59	H_2SO_4

η_t: quantum efficiency by temperature measurement.
η_a: quantum efficiency by actinometry.
s: single crystal.
p: polycrystal.

Table 2 Comparison of internal quantum efficiencies for current doubling reactions[15]

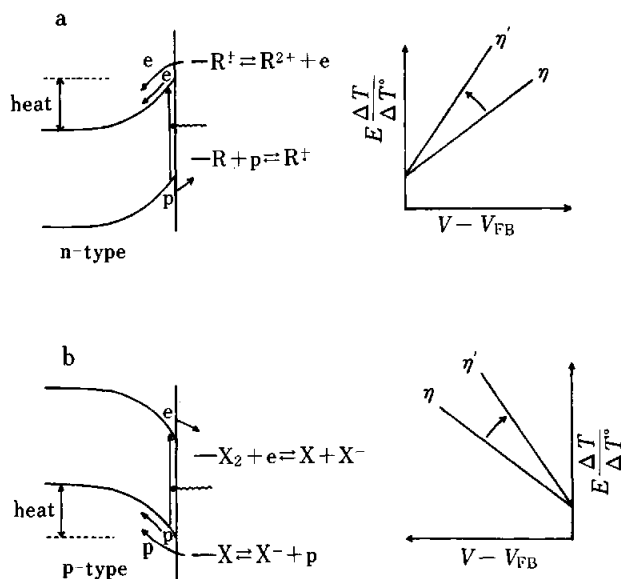| Electrode	Electrolyte	Reagent	$\eta^{(B)}_{max}$
n-ZnO p	Na_2SO_4	HCOOH	1.8
n-CdS s	Na_2SO_4	HCOOH	1.7
n-TiO$_2$ s	Na_2SO_4	HCOOH	0.7
p-GaP s	H_2SO_4	$(NH_4)_2S_2O_8$	1.5

s: single crystal.
p: polycrystal.

Fig. 5 The mechanism of current doubling, and the relation between PTS signal and applied bias for (a) n-type, and (b) p-type semiconductor. η and η' are internal quantum efficiencies obtainable from the plots of Eq. (23) for both n-type (a) and p-type (b) photoelectrodes in the absence, and in the presence of a current doubling reagent, respectively.
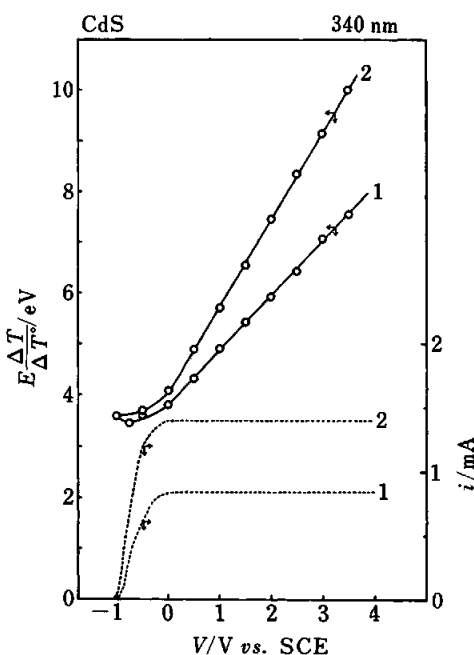

Fig. 6 Normalized PTS signal change vs. potential and photocurrent vs. potential of a n-CdS single crystal electrode.[15] Curves 1: 0.1 M Na_2SO_3 in 0.2 M Na_2SO_4; curves 2: 0.5 M HCOONa in 0.2 M Na_2SO_4. From the slopes of $\eta^{(B)}_{Qi}$ (V): curve 1, $\eta^{(B)}_{Qi}=1.0$; curve 2, $\eta^{(B)}_{Qi}=1.7$ (reprinted by permission of the Electrochemical Society, Inc.).

X and X⁻ photoproducts. X subsequently injects a hole in the valence band, Fig. 5(b). Theoretically, in these cases $\eta_{Qi}^{(B)}=2.0$. Experimentally, various semiconducting photoelectrodes gave quantum efficiencies between 1 and 2, with the exception of TiO_2 in Na_2SO_4 containing HCOONa, which yielded considerably smaller $\eta_{Qi}^{(B)}$, as shown in Table 2. No explanation for this low current doubling effect in the TiO_2–HCOONa system could be advanced by Maeda et al.[15] A typical plot showing the effects of current doubling mechanism is shown in Fig. 6. Those authors speculated that the cause of the experimental quantum efficiency values being less than two (Table 2) must be sought in the non-ideal injection of carriers by intermediate species (e.g. HCOO· in the n-CdS case).

Alongside the determination of $\eta_{Qi}^{(B)}$, the PTS-adapted Eq. (23) may also be used to quantify the $\eta_{Ei}^{(B)}$ value. Maeda et al.[7] utilized the (very good) approximation Eq. (19) with $\eta_{Qi}^{(B)}=1.0$ to calculate the ideal maximum

Table 3 Internal energy (conversion) efficiencies for the photo-oxidation of several redox agents on n-ZnO (p) electrode[7] at 3.6 eV irradiation

Redox agent	E_R vs. SCE[a]/V	$S_{intercept}^{(B)}$/ eV	$\eta_{Ei}^{(B)}$, %	$(\eta_{Ei}^{(B)})_{ideal}$, %
S^{2-}	−0.72	3.50	2.8	7.9
SO_3^{2-}	−0.22	3.25	10.8	10.7
$S_2O_3^{2-}$	−0.16	3.15	12.5	12.2
H_2O	+0.08	2.85	20.8	16.1

$$\eta_{Ei}^{(B)}=\frac{3.6-S_{intercept}^{(B)}}{3.6}\times100\%.$$

$$(\eta_{Ei}^{(B)})_{ideal}=\frac{|E_{FB}-E_R|}{3.6}\times100\%.$$

a. saturated calomel electrode.

internal energy efficiencies of polycrystalline ZnO semiconductor photoelectrodes in 0.2 M Na_2SO_4 electrolyte solution containing various redox agents. For those calculations they multiplied the maximum internal quantum efficiency, obtained from the slope of the PT vs. bias curve (see Fig. 3), and the maximum value of the photovoltage under monochromatic irradiation. Results are shown in Table 3, which also contains the values of the internal energy conversion efficiency. Evaluation of the intercept, $S_{intercept}^{(B)}$, Eq. (15), adapted to the PTS Eq. (23) yields

$$\eta_{Ei}^{(B)}\approx1-S_{intercept}^{(B)} \qquad (26)$$

from Eq. (20), assuming the entropy term to be negligible.[7] Fujishima et al.[11] have further used Eq. (20), including the entropy term, to calculate $\eta_{Ei}^{(B)}$ for the PEC systems $CdS/Fe(CN)_6^{3-}/Fe(CN)_6^{4-}$ and TiO_2/H_2SO_4. The entropy effect term was calculated from thermodynamic considerations and Eq. (26) gave $\eta_{Ei}^{(B)}=0.4$ (or 40%) for the CdS electrode ($\eta_{max}^{(B)}=1.0$), and 0.37 (or 37%) for the TiO_2 electrode ($\eta_{max}^{(B)}=0.7$). The largest $\eta_{Ei}^{(B)}$ was found to be accompanied by the largest $\eta_{Ei}^{(B)}$, as expected. It should be noticed that any accurate evaluation of $\eta_{Ei}^{(B)}$ requires the extrapolation of the PTS vs. ($V-V_{FB}$) curve to obtain the intercept and good knowledge of the entropy term, which must be evaluated independently or under normalization with the flatband-level signal. This matter will be taken up in Section 3·3.

3·2 Photothermal deflection spectroscopy (PDS)

Recently, PDS has emerged as a very suitable non-contact photothermal technique for quantum efficiency studies at the semiconductor-electrolyte interface. The main advantages of PDS over PTS are a) its non-
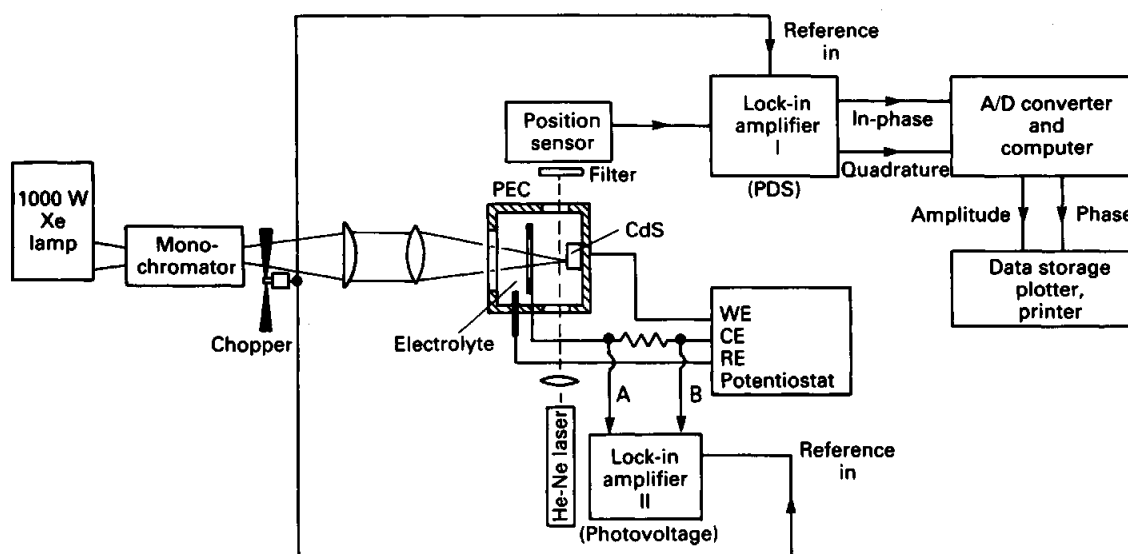

Fig. 7 Experimental apparatus for combined PDS and PCS measurements.[16]

intrusive nature (a mirage-effect optical probe beam, compared to the need for a physically contacting thermistor probe in PTS), and b) the much faster response time of PDS can accommodate modulated optical excitation of a photoelectrode and synchronous detection, which can improve dramatically the signal-to-noise ratio (SNR) of the PEC experiment. As a precursor to quantitative measurements, combined PDS and photocurrent spectroscopy (PCS) studies of single crystalline n-CdS-polysulfide electrolyte (1 M OH$^-$/1 M S^{2-}/1 M S) interfaces[16] have yielded *in-situ* self-consistent qualitative descriptions of energy-conversion mechanisms. Figure 7 shows a typical experimental apparatus for combined PDS and PCS PEC studies. Figure 8 gives a semi-qualitative description of the relative percentage contribution to the PDS signal from the interband nonradiative recombination compared with other current-flow related heating processes pertinent to the PEC reaction[16],

$$CdS \xrightarrow{h\nu} Cd^{2+}(aq.)+S(s)+2e^-. \qquad (27)$$
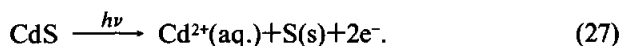
The nonradiative component anti-correlates with the photocurrent, while the other thermal components correlate with the photocurrent, as expected.[11] The nonradiative component *vs.* applied bias in Fig. 8 agrees well with the photoluminescent emission dependence on bias, explored[17] in a similar PEC experiment with CdS. This correlation between radiative and nonradiative processes is to be expected, since they constitute complementary carrier de-excitation pathways to the current-producing electron-hole separation.

The adaptation to PDS of Eq. (13) for the normalized, photothermal signal under bias has been presented by Wagner and Mandelis[8,9],

$$PDS_n^{(B)}(V)=[(h\nu-E_g)+(1-\eta_{Qi}^{(B)})E_g+\eta_{Qi}^{(B)}(E_R-E_{VB}^S)$$
$$+\eta_{Qi}^{(B)}|e|(V-V_{FB})+\eta_{Qi}^{(B)}T\Delta S]/h\nu. \qquad (28)$$

These authors further extended the PTS practice of calculating the maximum internal quantum efficiency, $\eta_{max}^{(B)}$, from the slope of the straight line, Fig. 3, and subsequently evaluating the term $(E_R-E_{VB}^S)+T\Delta S$ from the extrapolated intercept.[11] They showed the validity of Eq. (16) for all external biases[8] and used a combination of the $\eta_{max}^{(B)}$ and $(E_R-E_{VB}^S)+T\Delta S$ terms evaluated from the $PDS_n^{(B)}(V)$ slope and intercept, respectively, in conjunction with Eqs. (16) and (28) and experimental photocurrent data for $i_B(V)$ and i_{max}, to construct semi-theoretical fits of $PDS_n^{(B)}(V)$ curves to
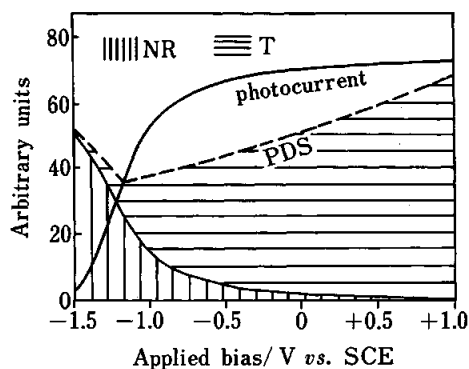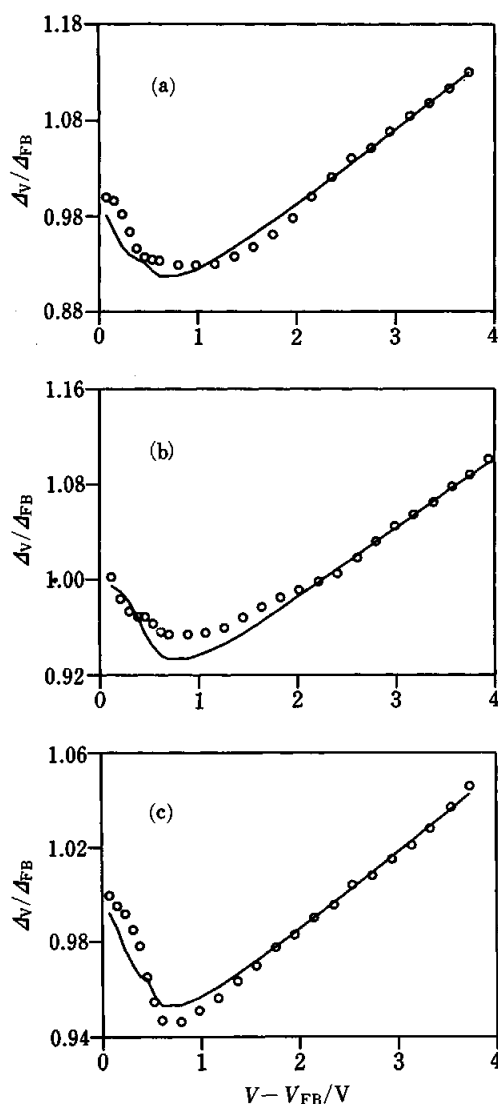
Fig. 8 Semi-qualitative curves comparing relative contributions to PD signal with photocurrent. NR, interband nonradiative de-excitation; T, other thermal processes in n-CdS in polysulfide electrolyte (see Fig. 1). The NR curve is in qualitative agreement with Fig. 5(a) in Streckert *et al.*[17] Any photodecomposition of the electrode was assumed to be negligible.[16]

Fig. 9 Experimental (-O-O-O-) and semi-theoretical (—) $PDS_n^{(B)}(V)\equiv\Delta v/\Delta_{FB}$ *vs.* $(V-V_{FB})$ curves for CdS in 0.01 M PS and f=25 Hz: (a) F-CdS, 490 nm; (b) Ga-CdS, 490 nm; (c) LR-CdS, 480 nm. (see Table 4).[9] Note that PDS$^{(B)}$ (V) data were normalized by the flatband PDS signal, since the photocurrent quantum efficiency is zero in both cases.

experimental data. The term "semi-theoretical" was coined to indicate that component values in the theoretical $PDS_n^{(B)}(V)$ curve were obtained from experimental data, rather than from theory. The resulting

Table 4 $\eta_{max}^{(B)}$ and $(E_R-E_{VB}^S)+\Delta G$ values determined from PDS vs. bias measurements in 0.01 M PS[9]

Electrode (doped-CdS)	$\lambda/$ nm	V_{FB} vs. SCE/V	$\eta_{max}^{(B)}$	$(E_R-E_{VB}^S)$ $+\Delta G$/eV
F-CdS	490	−1.55	0.20	0.31
Ga-CdS	490	−1.60	0.15	0.14
Ga-CdS	480	−1.60	0.24	−0.19
LR-CdS s	480	−1.55	0.09	−0.06

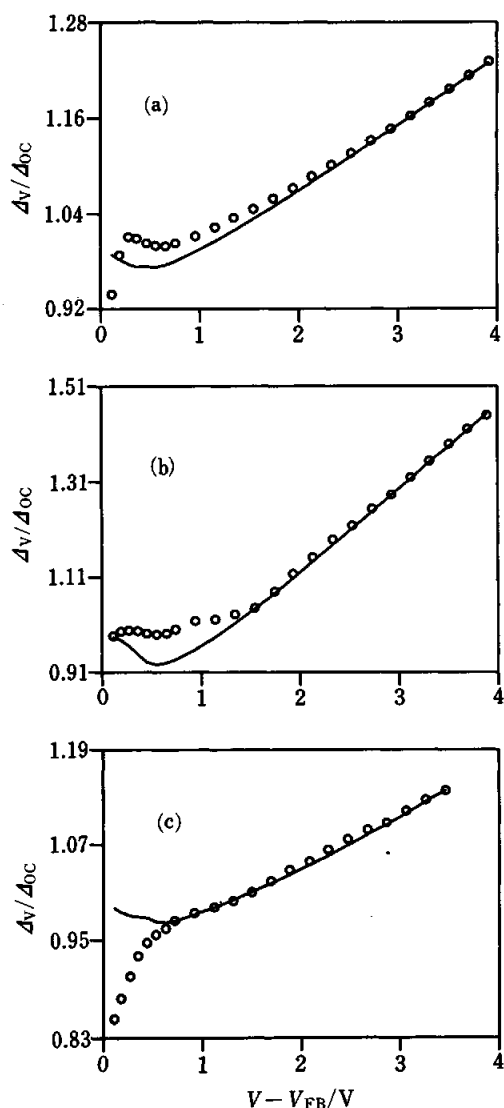LR: low resistivity (4.75 Ω cm, nominal).
s: single crystal.

Fig. 10 Experimental (O-O-O) and semi-theoretical (——) $PDS_n^{(B)}(V)\equiv\Delta v/\Delta_{OC}$ vs. $(V-V_{FB})$ curves for CdS in 0.05 M PS and $f=25$ Hz: (a) F-CdS, 480 nm; (b) Ga-CdS, 480 nm; (c) LR-CdS, 490 nm (see Table 5).[9]

curves thus extended the quantitative measurements introduced earlier[11,13] to the entire bias range, rather than one limited linear regime (slope) and the $V=V_{FB}$ point (intercept). Figure 9 shows experimental and semi-theoretical $PDS_n^{(B)}(V)$ vs. $(V-V_{FB})$ plots for three semiconductors. Table 4 shows the calculated values of $\eta_{max}^{(B)}$ and $(E_R-E_{VB}^S)+\Delta G$ obtained from the experimental curves in 0.01 M polysulfide electrolyte; (1 M OH⁻/0.01 M S²⁻/1 M S)≡0.01 M PS. It ought to be observed from Table 4 that all of the $\eta_{max}^{(B)}$ values were quite low compared to those of Table 1. This discrepancy was attributed[9] to photocorrosion, which dramatically affected the photoelectrodes in 0.01 M PS.

Figure 9 indicates the relatively good agreements between the experimental and semi-theoretical curves for all three semiconductor photoelectrodes, including the position of the $PDS_n^{(B)}(V)$ minimum on the $(V-V_{FB})$ axis. Figure 10 shows similar experimental curves and semi-theoretical fits for CdS photoelectrodes in 0.05 M polysulfide electrolyte; (1 M OH⁻/0.05 M S²⁻/ 1 M S)≡0.05 M PS. Here, the correlation between experimental and semitheoretical curves is best at high bias. The experimental curves exhibited anomalous downturns as the bias was decreased toward V_{FB}. This effect was attributed to photogenerated electrochemical species gradients, which would tend to push the probe beam away from the electrode, decreasing the thermal-wave PD signal.[18] This hypothesis was corroborated by the observation of large dc forward-bias currents in the 0.05 M PS electrolyte.[9] No such currents could be found in the 0.01 M PS. With regard to $\eta_{max}^{(B)}$ and $(E_R-E_{VB}^S)+\Delta G$ data, Table 5, an increase in $\eta_{max}^{(B)}$ was observed with decreasing wavelength, in agreement with the Gartner model[19] for PEC-like systems.

At the time of the writing of this review the heat generation model of Eqs. (1), (4), (6), (8) and (10) has been employed to derive a PDS-adapted expression for the normalized signal under external load[9],

Table 5 $\eta_{max}^{(B)}$ and $(E_R-E_{VB}^S)+\Delta G$ values determined from PDS vs. bias measurements in 0.05 M PS[9]

Electrode (doped-CdS)	$\lambda/$ nm	V_{FB} vs. SCE/V	$\eta_{max}^{(B)}$	$(E_R-E_{VB}^S)$ $+\Delta G$/eV
F-CdS	515	−1.50	0.10	0.76
F-CdS	510	−1.50	0.16	0.83
F-CdS	490	−1.50	0.21	1.09
F-CdS	480	−1.56	0.21	1.33
Ga-CdS	500	−1.50	0.19	1.49
Ga-CdS	490	−1.55	0.35	1.35
Ga-CdS	480	−1.55	0.44	1.15
Ga-CdS	470	−1.45	0.44	1.77
LR-CdS s	490	−1.53	0.16	1.10

LR: low resistivity (4.75 Ω cm, nominal).
s: single crystal.

$$PDS_n^{(L)} \equiv \frac{PDS^{(L)}}{PDS_{OC}} = [h\nu + (\eta_{Qi;ac}^{(L)} - \eta_{Qi;dc}^{(L)})E_g$$

$$-2(\eta_{Qi;ac}^{(L)}E_L^{dc} + \eta_{Qi;dc}^{(L)}E_L^{ac}) + 2\eta_{Qi;ac}^{(L)}\Delta G]/h\nu, \qquad (29)$$

where all quantities have been defined previously. An internal energy (conversion) efficiency under an external resistive load has also been defined and an expression derived[9] along the lines of Eq. (20) and using considerations similar to those employed by Cahen[20] for finding the internal energy conversion efficiency of a solid-state photovoltaic cell,

$$\eta_{Ei}^{(L)} = 1 - PDS_n^{(L)} = [2(\eta_{Qi;ac}^{(L)}E_L^{dc} + \eta_{Qi;dc}^{(L)}E_L^{ac})$$

$$-(\eta_{Qi;ac}^{(L)} - \eta_{Qi;dc}^{(L)})E_g - 2\eta_{Qi;ac}^{(L)}\Delta G]/h\nu. \qquad (30)$$

From the complicated form of Eq. (30) and the observed weak dependence of the PD signal on an external resistive load inserted in the PEC cell circuit of a CdS-polysulfide interface[9], it appears that the PDS technique is not well suited for determining the $\eta_{Ei}^{(L)}$ of PEC cells. The key experimental obstacle has been judged to be the presence of a photogenerated species gradient in the electrolyte, which may perturb the thermal-wave PD signal severely (see Fig. 10), making it difficult to observe small signal variations due to optical-to-electrical energy conversion efficiency changes with varying external load. The $\eta_{Ei}^{(L)}$ determination by PTS described in Section (a) above seems to be simpler than PDS in its interpretation, because it is not dependent on liquid-phase concentration gradients and it requires only a dc current or voltage component to be dealt with for the analysis. Unfortunately, no PT measurements of $\eta_{Ei}^{(L)}$ have been reported to-date. On the other hand, the PD experiments described above[8,9] were performed with the PEC cells connected to potentiostats. The concept of a PEC cell energy efficiency, $\eta_{Ei}^{(B)}$, has little meaning in this context, since under potentiostatic conditions the PEC cell is effectively at short circuit.

3·3 Photoacoustic spectroscopy (PAS)

Photoacoustic detection can be effected through one of two conventional methods:[1] either by means of a piezoelectric transducer in intimate contact with the sample under investigation, or remotely by means of a coupling gas in a hermetically sealed cell and a microphone sensitive to pressure changes in the gas due to the photoacoustic effect.[1] A typical experimental set-up of the piezoelectric PA detection head is shown in Fig. 11. The rest of the apparatus was similar to the one shown in Fig. 2(a). A lead-zirconate-titanate (PZT) transducer has been used to measure the internal quantum efficiencies of n-type[21] and p-type[22] semiconductor electrodes. When adapted to photoacoustic signal measurements, Eq. (13) may be written as[21]

$$E\left(\frac{\Delta P}{\Delta P_{OC}}\right) = \eta_{Qi}^{(B)}(V - V_{FB}) + \frac{1}{N\tau}(Q_{SC} + T\Delta S), \qquad (31)$$

where ΔP and ΔP_{OC} are the PA signal amplitudes from the piezoelectric transducer at bias V and at open-circuit, respectively. All other symbols were defined earlier. Experimentally, ohmic contacts are made to one side of the semiconductor photoelectrode for carrying the photocurrent to the detection electronics. The PA transducer is attached to the same side after interposing a thin insulating layer, Fig. 11. The entire electrode, except for the front surface, is covered with an electrolyte-resistant layer (e.g. epoxy resin). Figure 12 shows the PA signal dependence on applied bias for a n-CdS photoelectrode. Table 6 summarizes results obtained from n-type and p-type crystals. The data shown in Table 6A are, generally, in good agreement with values for $\eta_{Qi}^{(B)}$ obtained earlier by the same group using PT detection.[11,13,15,23] The electrochemical systems shown in Table 6A were as follows:
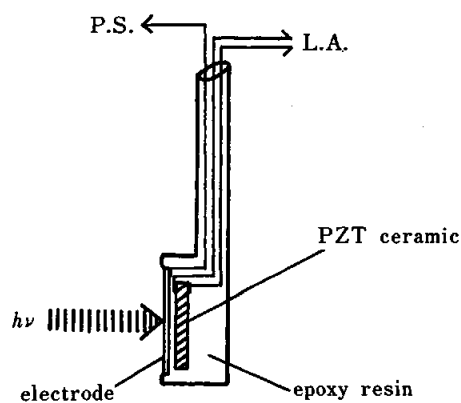

Fig. 11 Schematic of the photoelectrode-PZT detector assembly for PA measurements in semiconductor PEC cells. P.S., potentiostat; L.A., lock-in amplifier (reprinted by permission of the Chemical Society of Japan).[21]
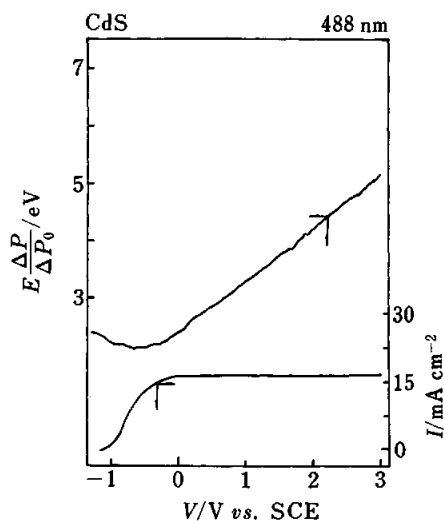

Fig. 12 Photocurrent and PA dependence on applied potential for a n-CdS photoelectrode in a 0.2 mol/dm³ Na₂SO₄, 1 mol/dm³ Na₂SO₃ aqueous electrolyte.[21] Light intensity modulation frequency: 10 Hz (reprinted by permission of the Chemical Society of Japan).

501

Table 6A Measured internal quantum efficiencies for n-TiO₂, n-CdS and n-ZnO by photoacoustic spectroscopy; ( ) stands for the value in the case of current doubling reaction[21]

	Saturation current[a]/ mA cm⁻²	Quantum efficiency[c] $\eta_{Qi}^{(B)}$
n-TiO₂[b]	5.44	0.8±0.05
	(6.24)	(1.0±0.05)
n-CdS	16.4	0.9±0.01
	(28.0)	(1.5±0.01)
n-ZnO	2.72	0.8±0.1
	(5.36)	(1.5±0.1)

a. For TiO₂ and ZnO relatively low power He-Cd laser (325 nm) and for CdS high power Ar-ion laser (488 nm) were used.

b. TiO₂ electrode was prepared by thermal oxidation of Ti metal plate.

c. To be compared with PTS values in Table 1. ( ) to be compared with current doubling PTS values in Table 2.

Table 6B Experimental values of internal quantum efficiency for hydrogen evolution reaction on Pt plated p-InP photoelectrode[22]

| The number of Pt layers[a]	1/100	1/10	1
The quantum efficiency	0.48	0.57	0.53

a. On the assumption of uniform deposition of Pt (in fact deposited Pt was dispersed like islands).

(1) n-TiO₂/Na₂SO₄, aq.
       $(4OH^- \longrightarrow O_2 + 2H_2O + 4e^-)$

(2) n-CdS/Na₂SO₄, Na₂SO₃, aq.
       $(2SO_3^{2-} + 2p^+ \longrightarrow S_2O_6^{2-})$

(3) n-ZnO/Na₂SO₄, aq.
       $(2ZnO + 4p^+ \longrightarrow 2Zn^{2+} + O_2)$

(4) n-TiO₂/Na₂SO₄, HCOONa, aq.
       $(p^+ + HCOO^- \longrightarrow CO_2 + H^+ + e^-)$;
                  (current doubling reaction)

(5) n-CdS/Na₂SO₄, HCOONa, aq.
       $(p^+ + HCOO^- \longrightarrow CO_2 + H^+ + e^-)$;
                  (current doubling reaction)

(6) n-ZnO/Na₂SO₄, HCOONa, aq.
       $(ZnO + 2p^+ + 2HCOO^- \longrightarrow$
                  $Zn^{2+} + H_2O + 2CO_2 + 2e^-)$;
                  (current doubling reaction)

As far as the cathodic PEC reaction using a Pt-plated p-InP photoelectrode is concerned, Table 6B, the PA signals were found[22] to be adequate for quantitative analysis of $\eta_{Qi}^{(B)}$; however, the results shown with Ar⁺-ion laser excitation at 488 nm *appear to be* of lower quality than other equivalent PTS or PDS data

presented earlier. Through their PZT-PA probe, Yoshihara and Fujishima[22] were not able to confirm earlier reports by Szklarczyk and Bockris[24] of a quantum efficiency larger than unity for H₂ evolution reaction on Pt-plated p-InP.

Microphonic PA detection of semiconductor photoelectrochemistry has been performed by Dohrmann's group in the back-detection mode. The experimental set-up was essentially similar to the one presented in Fig. 7 for combined PA and photocurrent monitoring. The main departure from that geometry lay in the positioning of a microphone attached to the back surface of an electrode, as detailed elsewhere.[25] For such measurements, no front surface PA detection is possible, due to the exponential decay of the PA signals from the photoelectrode surface in the bulk of the overlying transparent electrolyte.[26] Sample electrodes must also be chosen to be thin, so that PA detection will occur in the thermally thin regime for optimum SNR considerations.[26] Rappich and Dohrmann[27] have monitored the oxidation reaction,

$$4h^+(TiO_2) + 2H_2O \longrightarrow O_2(g) + H_{aq}^+, \tag{32}$$
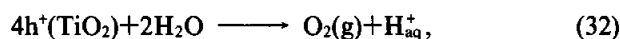
in 0.5 M H₂SO₄ at various electrode potentials. From Eqs. (13) and (15), re-definition of the signal variable to reflect adaptation to the photoacoustic signal, and signal normalization with the flatband (rather than the open-circuit) value, yield

$$L(V) \equiv \frac{P(V) - P(V_{FB})}{P(V_{FB})}$$

$$= \eta_{Qi}^{(B)}(V) \left[\frac{|e|(V - V_R) + \Delta G}{E} \right], \tag{33}$$

where $|e|V_R = E_R$ (the redox potential), and all other symbols have been defined earlier. The flatband potential is a very convenient reference value, because $\eta_{Qi}^{(B)}(V_{FB}) = 0$ (as at open-circuit) and only processes Eqs. (1) and (2) contribute to the PA signal. In Eq. (33) the EPH term ΔG has been defined in detail as[27]

$$\Delta G = -T(\Delta S_R + \Delta S_t + \Delta S_{e^-}) + \Delta G_t, \tag{34}$$

associated with entropy changes ΔS_R, ΔS_t and ΔS_{e^-} for the photoanodic net reaction, the charge carrier transport in the semiconductor, and the electron transfer (n-type electrodes) across the semiconductor-metal junction, respectively. ΔG_t is the EPH component due to heat released following ionic transport upon participation in the electrode reaction.[28] By using the normalization indicated in Eq. (33), the authors were able to obtain $L(V)$ vs. V curves resembling those obtained by PTS, Fig. 3. Further determination of the potential V_0 at which $L(V_0) = 0$ yielded the value $V_0 - V_R = 0.27$ V for the reaction (32) and the EPH was found to be $\Delta G = -0.27$ eV per hole transferred in that
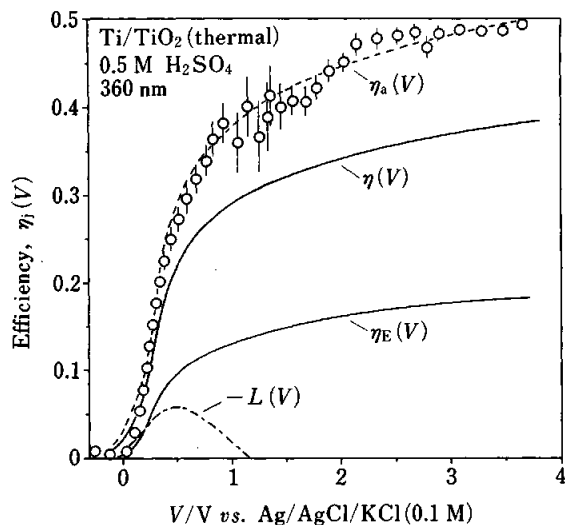
V/V $vs.$ Ag/AgCl/KCl(0.1 M)

Fig. 13 Internal quantum efficiency, $\eta_{Qi}^{(B)} \equiv \eta_a(V)$, external quantum efficiency, $\eta(V)$, and energy conversion efficiency, $\eta_{Ei}^{(B)} \equiv \eta_E(V)$, for the photoanodic oxidation of water at the TiO$_2$ (rutile) thin-film electrode. Open circles: $\eta_a(V)$ as determined from Eq. (33); $\eta_E(V)$ and $\eta_E'(V) = -L(V)$ as determined from Eqs. (19) and (36), respectively.[27] Optimum anode potential for photoanodic water oxidation is 0.5 V ($\eta_E = 0.1$) (reprinted by permission of VCH Publischers, Inc.).
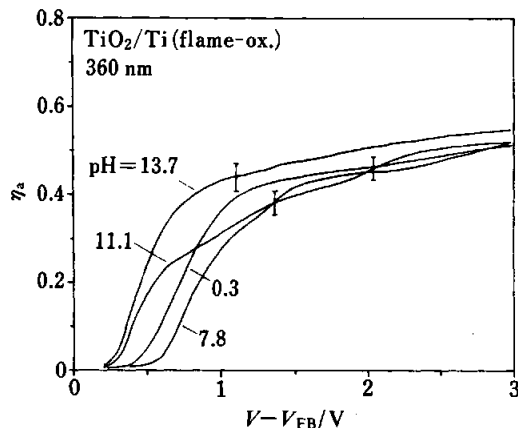

Fig. 14 Internal quantum efficiency of the photocurrent $vs.$ band bending ($V - V_{FB}$) for the TiO$_2$ electrode at 360 nm in solutions at different pH as obtained from Eq. (33) (reprinted by permission of the American Chemical Society).[30]

reaction. Finally, insertion of these values in Eq. (33) gave the potential dependence of the internal quantum efficiency throughout the entire bias range. The results are shown in Fig. 13, which also shows the functional dependence of the *external* quantum efficiency, $\eta_{Qe}^{(B)} \equiv \eta(V)$ at 360 nm as measured at the TiO$_2$ thin-film electrode independently. The larger values of $\eta_{Qi}^{(B)}$ ($=1.3\eta$) have been attributed to the reflectivity, R, of the electrode/ electrolyte interface,

$$R = 1 - (\eta_{Qi}^{(B)} / \eta_{Qe}^{(B)}). \tag{35}$$

Figure 13 further shows the internal energy conversion efficiency, $\eta_{Ei}^{(B)} \equiv \eta_E(V)$ according to Eq. (19). Inclusion in Eq. (19) of the EPH term ($\Delta G/E$) and the Joule heat term $|e|(V - V_{FB})$ evolved in the photoelectrode during photoelectrolysis, can be shown[27] to yield the expression (see Eq. (20)),

$$\eta_E'(V) = -L(V), \tag{36}$$

where $L(V)$ is given by Eq. (33). This quantity is also shown in Fig. 13. The onset of negative values for $\eta_E'(V)$ is at $V = 1.18$ V, indicating the increasing contribution of the Joule heat which represents a loss of external applied electrical energy in the photoanode.

Rappich and Dohrmann have monitored the PA signal and photocurrent in the manner described above in a slight variant of the system of reaction (32).[29] This application involved a passivated 0.1 mm Ti foil electrode (0.3 μm TiO$_2$ formed at 100 V) during a

voltage scan in 0.5 M Na$_2$SO$_4$ at pH 7. Results very similar to those shown in Fig. 13 were thus obtained. A recent very interesting PEC study of the pH dependence of the internal quantum efficiency and of the EPH for the n-TiO$_2$ (rutile) thin-film electrode in aqueous Na$_2$SO$_4$ solution at various pH values (0.3 – 13.7) has been presented by those same authors[30] using the back-detection microphonic PA technique. Figure 14 shows the internal quantum efficiency dependence on the pH, calculated from Eq. (33). In alkaline solutions the following net photoanodic reaction is expected:

$$4OH^- + 4h^+ \longrightarrow O_2 + 2H_2O. \tag{37}$$
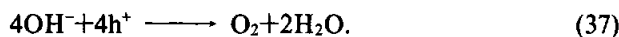
With increasing pH values there is a shift of the $\eta_{Qi}^{(B)}(V) \equiv \eta_a(V)$ curves in Fig. 14 toward lower band bending. This is indicative of a decrease in the rate of electron-hole surface recombination and/or an acceleration of the charge-transfer process with increasing concentration of OH$^-$ ions, a well-known fact from earlier non-photothermal studies.[31] Further manipulation of the data presented in Fig. 14 showed that the quantum efficiencies (internal *and* external) do not significantly depend on the pH in the saturation range of the photocurrent, $V - V_{FB} \approx 3$ V. The ability of the particular normalization method, Eq. (33), used by Rappich and Dohrmann to measure the EPH *in situ* led to a detailed analysis of the contributions of the various Peltier heat components, Eq. (34), to the pH-dependent PA signal.[30] Their study has allowed the calculation of the pH ranges for the different net reactions (acidic or alkaline) of the photoanodic oxidation of water at the TiO$_2$ electrode. This kind of information cannot be obtained directly from photocurrent-potential curves and shows the advantages of using PAS to study competing PEC reactions.

4 Summary

This review has presented important progress to-date in the field of PEC cell thermodynamic parameter measurements (internal quantum efficiency and internal energy conversion efficiency) by means of photo-thermal-wave detection. PTS appears to be experimentally sensitive and theoretically simple to interpret; however, the sample surface must be in contact with a thermistor, the risetime of which is generally too long for modulated photothermal excitation. As a consequence, only dc measurements can be realistically achieved at the expense of low SNR. This consideration, coupled with the front-surface intrusive nature of the technique, has limited its popularity in recent years. PDS is, on the other hand, a non-contact, non-intrusive technique, with the added virtue of very fast risetimes and, thus, is very suitable for modulated excitation and lock-in detection. Its application to semiconductor photo-electrochemistry has shown abilities similar to PTS in terms of internal quantum efficiency measurements under bias. Sensitivity to electrochemical concentration gradients and an observed weak dependence of PD signals on external resistive load have been the causes of the lack of measurements of quantum efficiencies and energy conversion efficiencies under load conditions of the PEC interface. Piezoelectric photoacoustic detection has been shown to yield information similar to PTS and PDS, albeit of a lower quality, as judged by this author upon surveying published curves to-date. The required special sample preparation and encasing represents a disadvantage. The need to have a rigid intimate contact with the piezoelectric transducer renders this method the most intrusive of all photothermal techniques. Back-surface microphonic PAS seems to offer a better alternative in terms of sensitivity and non-intrusiveness at the PEC interface, yet, it requires a relatively sophisticated set-up due to its back-detection nature and the need for hermetic sealing of the PA cell. It appears that PDS exhibits a majority of advantages regarding in-situ photothermal measurements of the PEC interface. With the appropriate signal normalization and reference conditions, photothermal detection techniques can offer good quantitative information on internal quantum and energy efficiencies, as well as simple and sensitive measurements of the electrochemical Peltier heat of the photoelectrode reaction.

References

1. A. Rosencwaig, "Photoacoustics and Photoacoustic Spectroscopy", Wiley Interscience, New York, 1980.
2. "Photothermal Investigations of Solids and Fluids", ed. J. A. Sell, Academic Press, New York, 1989.
3. A. Mandelis, in "Photothermal Investigations of Solids and Fluids", ed. J. A. Sell, Chap. 9, Academic Press, New York, 1989.
4. S. R. Morrison, "Electrochemistry at Semiconductor and Oxidized Metal Electrodes", Plenum Press, New York, 1980.
5. Yu, V. Pleskov and Yu. Ya. Gurevich, "Semiconductor Photoelectrochemistry" (P. N. Bartlett, Transl. Ed.), Consultants Bureau, New York, 1986.
6. J. I. Pankove, "Optical Processes in Semiconductors", Dover Publ., Inc., New York, 1971.
7. Y. Maeda, A. Fujishima and K. Honda, Bull. Chem. Soc. Jpn., 55, 3373 (1982).
8. R. Wagner and A. Mandelis, in "Photoacoustic and Thermal Wave Phenomena in Semiconductors", ed. A. Mandelis, Chap. 14, North-Holland, New York, 1987.
9. R. E. Wagner and A. Mandelis, Phys. Rev. B, 38, 9920 (1988-I).
10. M. Fujihira, T. Osa, D. Hursh and T. Kuwana, J. Electroanal. Chem. Interfacial Electrochem., 88, 285 (1978).
11. A. Fujishima, Y. Maeda, K. Honda, G. H. Brilmyer and A. J. Bard, J. Electrochem. Soc., 127, 840 (1980).
12. A. L. Fahrenbruch and R. H. Bube, "Fundamentals of Solar Cells", Academic Press, New York, 1983.
13. A. Fujishima, Y. Maeda and K. Honda, Bull. Chem. Soc. Jpn., 53, 2735 (1980).
14. J. M. Sherfey and A. Brenner, J. Electrochem. Soc., 105, 665 (1958).
15. Y. Maeda, A. Fujishima and K. Honda, J. Electrochem. Soc., 128, 1731 (1981).
16. R. E. Wagner, V. T. Wong and A. Mandelis, Analyst [London], 111, 299 (1986).
17. H. H. Streckert, J.-R. Tong, M. K. Carpenter and A. B. Ellis, J. Electrochem. Soc., 129, 772 (1982).
18. A. Mandelis and B. S. H. Royce, Appl. Opt., 23, 2892 (1984).
19. W. W. Gartner, Phys. Rev., 116, 84 (1959).
20. D. Cahen, Appl. Phys. Lett., 33, 810 (1978).
21. S. Yoshihara, A. Aruchamy and A. Fujishima, Bull. Chem. Soc. Jpn., 61, 1017 (1988).
22. S. Yoshihara and A. Fujishima, Mat. Res. Bull., 23, 759 (1988).
23. Y. Maeda, A. Fujishima and K. Honda, Chem. Lett., 1980, 271.
24. M. Szklarczyk and J. O'M. Bockris, J. Phys. Chem., 88, 5241 (1984).
25. U. Sander, H.-H. Strehblow and J. K. Dohrmann, J. Phys. Chem., 85, 447 (1981).
26. A. Mandelis, Y. C. Teng and B. S. H. Royce, J. Appl. Phys., 50, 718 (1979).
27. J. Rappich and J. K. Dohrmann, Ber. Bunsen-Ges. Phys. Chem., 92, 1342 (1988).
28. E. Lange and H. Göhr, "Thermodynamische Elektrochemie", Dr. Alfred Hüthig Verlag, Heidelberg, 1962.
29. J. Rappich and J. K. Dohrmann, in "Photoacoustic and Photothermal Phenomena", ed. P. Hess and J. Pelzl, p. 204, Springer-Verlag, Berlin, 1988.
30. J. Rappich and J. K. Dohrmann, J. Phys. Chem., 93, 5261 (1989).
31. P. Salvador, J. Electrochem. Soc., 128, 1895 (1981).